Single and double grating-based X-ray microtomography using synchrotron radiation

P. Thalmann, C. Bikis, A. Hipp, B. Müller, S. E. Hieber, and G. Schulz

Citation: Appl. Phys. Lett. **110**, 061103 (2017); doi: 10.1063/1.4975679
View online: http://dx.doi.org/10.1063/1.4975679
View Table of Contents: http://aip.scitation.org/toc/apl/110/6
Published by the American Institute of Physics

Single and double grating-based X-ray microtomography using synchrotron radiation

P. Thalmann,[1] C. Bikis,[1] A. Hipp,[2] B. Müller,[1] S. E. Hieber,[1] and G. Schulz[1]
[1]*Biomaterials Science Center, University of Basel, 4123 Allschwil, Switzerland*
[2]*Institute of Materials Research, Helmholtz-Zentrum Geesthacht, 21502 Geesthacht, Germany*

(Received 3 November 2016; accepted 20 January 2017; published online 6 February 2017)

Hard X-ray phase contrast imaging techniques have become most suitable for the non-destructive three-dimensional visualization of soft tissues at the microscopic level. Among the hard X-ray grating interferometry methods, a single-grating approach (XSGI) has been implemented by simplifying the established double-grating interferometer (XDGI). We quantitatively compare the XSGI and XDGI tomograms of a human nerve and demonstrate that both techniques provide sufficient contrast to allow for the distinction of tissue types. The two-fold binned data show spatial resolution of (5.2 ± 0.6) μm and (10.7 ± 0.6) μm, respectively, underlying the performance of XSGI in soft tissue imaging. *Published by AIP Publishing*. [http://dx.doi.org/10.1063/1.4975679]

X-ray grating interferometry (XGI) is a phase contrast imaging technique with distinctive contrast for applications and future developments in materials science, biomedical engineering, and beyond. Using synchrotron radiation, X-ray double-grating interferometry (XDGI) is one of the most powerful techniques in current use, due to its superior contrast, despite generally providing inferior spatial resolution compared to in-line methods.[1,2] Since the pixel size of commercially available detector modules is generally larger than the features of the obtained interference pattern from the beam-splitter grating g_1, grating interferometers often consist of two gratings, whereby the second one acts as an analyzer grating g_2.[3] The spatial resolution of such a set-up is limited by the periodicity of the analyzer grating.[3] Thus, the X-ray single-grating interferometer (XSGI) profits from easier handling, as only one grating has to be aligned, and from the related cost reduction. Most importantly, spatial resolution is not limited by the analyzer grating period, and for the same flux, the number of detected photons is increased by a factor of about two. Several research teams have performed phase tomography with a single-grating setup, including the proof of principle study by Takeda *et al.*[4] The three-page letter belongs to the first publications in the field and shows the feasibility of the approach. The explanations are corroborated by preliminary synchrotron radiation-based experiments on a two-component polymer with a limited field of view (FOV) of 1.3 mm^2. The authors mention in their proof-of-principle study 8 μm spatial resolution and a 9 mg/cm^3 detection limit of density deviation. As the authors only briefly explained how the quantities were derived, one has to consider them as estimates. It remains unclear how the refractive index deviation was evaluated from the noise. Thus, the letter is in line with the communications of other teams.[5] Furthermore, due to the small FOV, both settings used do not allow for a tomography of a centimeter-sized biomedical specimen with the necessary resolution of a few micrometers within a reasonable acquisition time. So far, there exists no detailed study on the quantitative evaluation of the XSGI performance in comparison to a well-established X-ray imaging technique.

For tissues, which are mainly composed of low atomic number elements, the phase-shift cross-section for X-rays is about 10^3 times higher than for the related absorption.[6,7] Therefore, X-ray phase contrast techniques exhibit superior contrast between internal anatomical structures within soft tissues not seen in standard absorption techniques.[8] In particular, peripheral nerves are attractive, because numerous animal models for nerve regeneration are available, and these studies often lack appropriate three-dimensional imaging with true micrometer resolution.[9,10] The models often rely on bio-engineered scaffolds, and here, detailed microstructural knowledge allows for targeted modification of the scaffolds' properties and biocompatibility.[11] Recent studies indicate that hard X-ray micro computed tomography, especially with synchrotron radiation, is well-suited to solve imaging tasks for animal models.[12,13] For the present communication, a human peripheral nerve was chosen, as the preparation procedure is standard in pathology, while the spatial resolution necessary to make the nerve anatomy visible is less ambitious than for the rodent peripheral nerve. The purpose of the present study is to make a direct comparison between XSGI and XDGI while analyzing a human peripheral nerve, which necessarily has to include both spatial resolution and the contrast-to-noise ratio (CNR).

The tomography measurements were carried out at the beamline P07 (PETRA III, DESY, Hamburg, Germany), operated by the Helmholtz-Zentrum Geesthacht.[14] An undulator source, in combination with a double-crystal monochromator consisting of two Si(111) Laue crystals on Rowland geometry, was used. Photon energy was set to 40 keV with an estimated photon flux of around 6×10^{13} $s^{-1}mm^{-2}$.

XSGI measurement was performed using a beam-splitter grating with a periodicity of $p_1^{(s)} = 4.8$ μm and a Si structure height of 7 μm, in order to induce a phase shift of $\pi/2$ for the photon energy selected. This results in self-images of the beam-splitter grating with a periodicity $p_1^{(s)}$ and maximal contrast at the fractional Talbot distances

$$d_n(\pi/2) = n\frac{p_1^2}{2\lambda}, \tag{1}$$

where n denotes an odd integer and λ denotes the wavelength of the incoming photons.[15]

The XDGI measurement was performed using a beam-splitter grating $g_1^{(d)}$ with a periodicity of $p_1^{(d)} = 4.8\,\mu$m and a Si structure height of $14\,\mu$m, typically used to achieve a phase shift of π.[16,17] The gold lines of the analyzer grating $g_2^{(d)}$ had a structure height of $\sim 100\,\mu$m with a periodicity of $p_2^{(d)} = 2.4\,\mu$m, corresponding to a transmission of only about 8%. The set-up for the XDGI measurement induces an interference pattern with a period $p_1^{(d)}/2$ and maximal contrast at the fractional Talbot distances

$$d_n(\pi) = n\frac{p_1^2}{8\lambda}, \tag{2}$$

where n is an odd integer.[15]

For both methods, we acquired 900 projections over 360°. At each projection angle, five phase-step images over one period of the interference pattern were recorded. With an exposure time of 140 ms per phase-step, this resulted in a scan time of almost 4 h. During camera readout and movement of the mechanical stages, the beam shutter was closed, in order to avoid unnecessary irradiation on the sample. The radiographs were recorded using a camera manufactured at the Institute for Data Processing and Electronics (Karlsruhe Institute of Technology, Karlsruhe, Germany) with a CMOS chip (CMOSIS, Antwerp, Belgium), featuring a 20 Megapixel (5,120 × 3,840) resolution with 6.4 μm-sized square pixels and a $100\,\mu$m thick $CdWO_4$ scintillator as an imaging detector. Both measurements were performed using a magnification of five, resulting in an effective pixel length of 1.3 μm.

For an adequate comparison of the two measurement techniques, the signal for both techniques should be comparable. Due to the gratings chosen, the inter-distance of the phase grating $g_1^{(s)}$ and the camera (C) had to be twice the distance $\overline{g_1^{(d)} g_2^{(d)}}$.[18] In addition, similar relative visibility from its respective maximum was achieved by the condition

$$\overline{g_1^{(d)} g_2^{(d)}}_{relativeVisibility} = \overline{g_1^{(d)} g_2^{(d)}}_{maximalVisiblity} - s, \tag{3}$$

$$\overline{g_1^{(s)} C}_{relativeVisiblity} = \overline{g_1^{(s)} C}_{maximalVisiblity} + 4 \times s, \tag{4}$$

where s denotes the distance away from maximal visibility.[15] Therefore, the distance between $g_1^{(d)}$ and $g_2^{(d)}$ was 248 mm, close to the third fractional Talbot order, and the distance between $g_1^{(s)}$ and C was 496 mm, close to the first fractional Talbot order. For the synchrotron radiation source, visibility

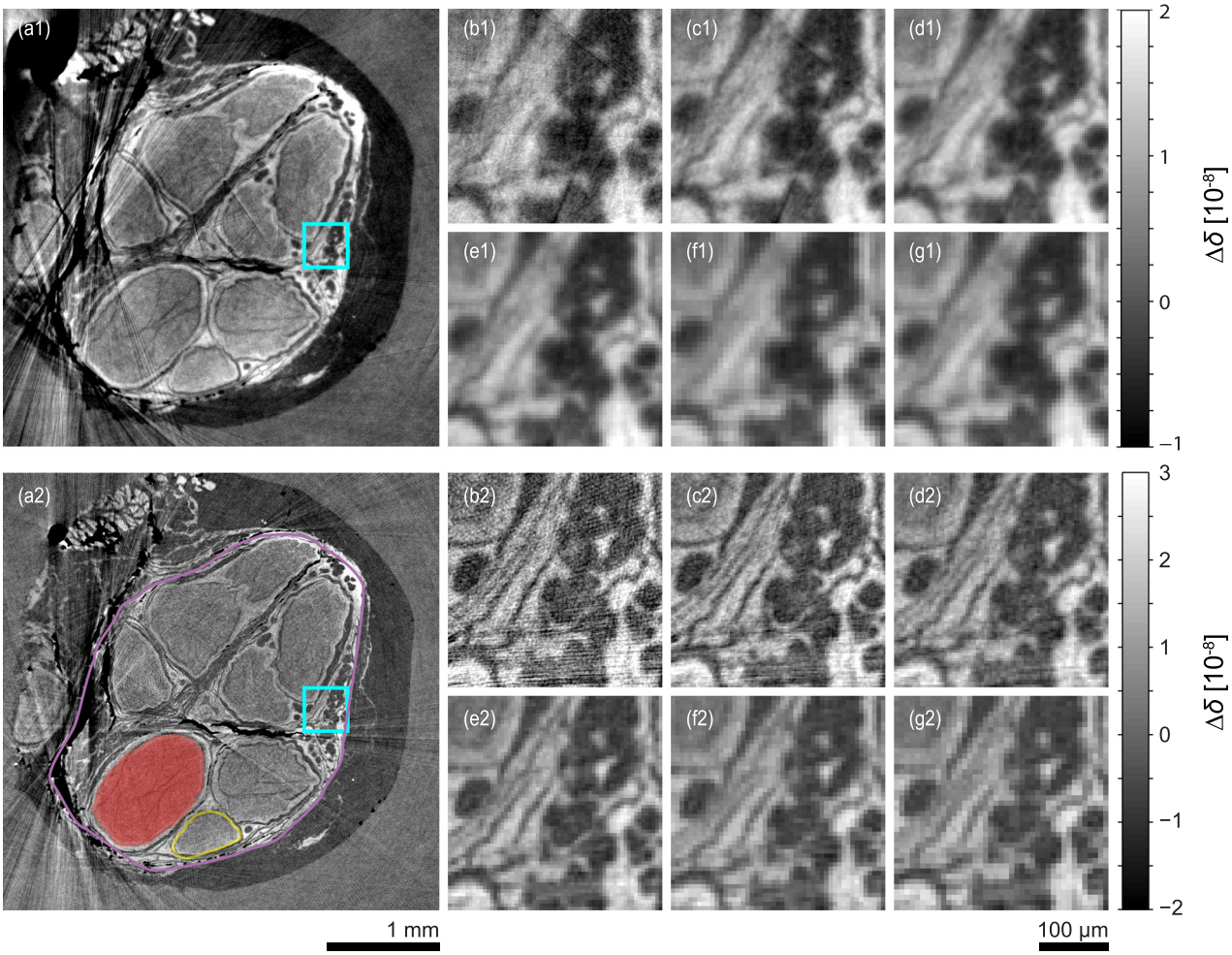

FIG. 1. X-ray phase tomography slice (a) of the human nerve using XDGI (top) and XSGI (bottom). The epineurium (violet), perineurium (yellow), and endoneurium (red) are clearly distinguishable for both techniques. The region enclosed by the cyan square is displayed for binning factors of 1 × 1 (b), 2 × 2 (c), 3 × 3 (d), 4 × 4 (e), 5 × 5 (f), and 6 × 6 (g). For both techniques, the grayscale bar was optimized for the respective figure displayed in (c), see also Fig. 2.

differences in the first fractional Talbot orders are negligible.[15]

The biological specimen used for the measurement was a human peripheral nerve, obtained post-mortem from a donated body. Informed consent for scientific use was obtained beforehand. All procedures were conducted in accordance with the Declaration of Helsinki and were approved by the Ethikkommission Nordwestschweiz. The peripheral nerve was extracted from the donated body and fixed in 4 % histological-grade buffered formalin. It was subsequently dehydrated and embedded in a paraffin/plastic polymer mixture, according to standard pathology procedure. The cylindrical sample for the tomography measurement was extracted from the paraffin block, using a metal punch with an inner diameter of 6 mm and was subsequently mounted on a specialized sample holder for the tomography data acquisition.

The phase-retrieved projections were achieved using a pixel-wise Fourier analysis. Then, the phase contrast tomograms were reconstructed using the standard filtered back-projection algorithm[19] implemented in Matlab® (2014a, The MathWorks, Inc., Natick, Massachusetts, USA) employing a modified filter kernel (Hilbert transform).[20] It has already been shown that the optimization of tomograms can be achieved using the optimized binning factor.[21] As we did not know this factor *a priori*, each dataset was reconstructed with the binning factors ($n \in \{1, ..., 6, 12\}$). We also verified that the sequence of the reconstruction process had no effect on the final results, by performing the binning at selected process steps along the reconstruction pipeline, namely, on the raw projections (only possible for XDGI), phase-retrieved images, and after integration. All three reconstruction sequences yielded almost identical results. Furthermore, we needed to account for the fact that the specimen was unmounted between the measurements. In detail, to compare the datasets for the applied binning factors, we performed rigid registration using a Powell optimizer and the Mattes mutual information metric. Translation registration was sufficient, since rotation invariance was assured by the mounting stage. For dataset resampling, we chose the nearest neighbor interpolator, so that the registration had no significant influence on the histogram of the floating image. Registration itself was performed using the library provided by ITK.[22]

Fig. 1 shows a characteristic slice of a human nerve provided by XDGI and XSGI, respectively. For both techniques, one can observe the main anatomical features of the nerve, wherein the epineurium, perineurium, and endoneurium are clearly distinguishable (see Fig. 1). Blood vessels are visible in the connective tissue, as well as nerve fascicles enclosed by the perineurium. The streak artefacts noticeable in both reconstructions originate from air-filled cracks in the paraffin. The XDGI images also contain prominent artefacts, due to air bubble formation during data acquisition. The most likely explanation is that the rougher paraffin surface allowed for the formation of micro air bubbles while inserting the specimen into the water tank, which then grow during irradiation. Therefore, smoothing of the paraffin reduces the artefacts from growing air bubbles at the paraffin surface.[23]

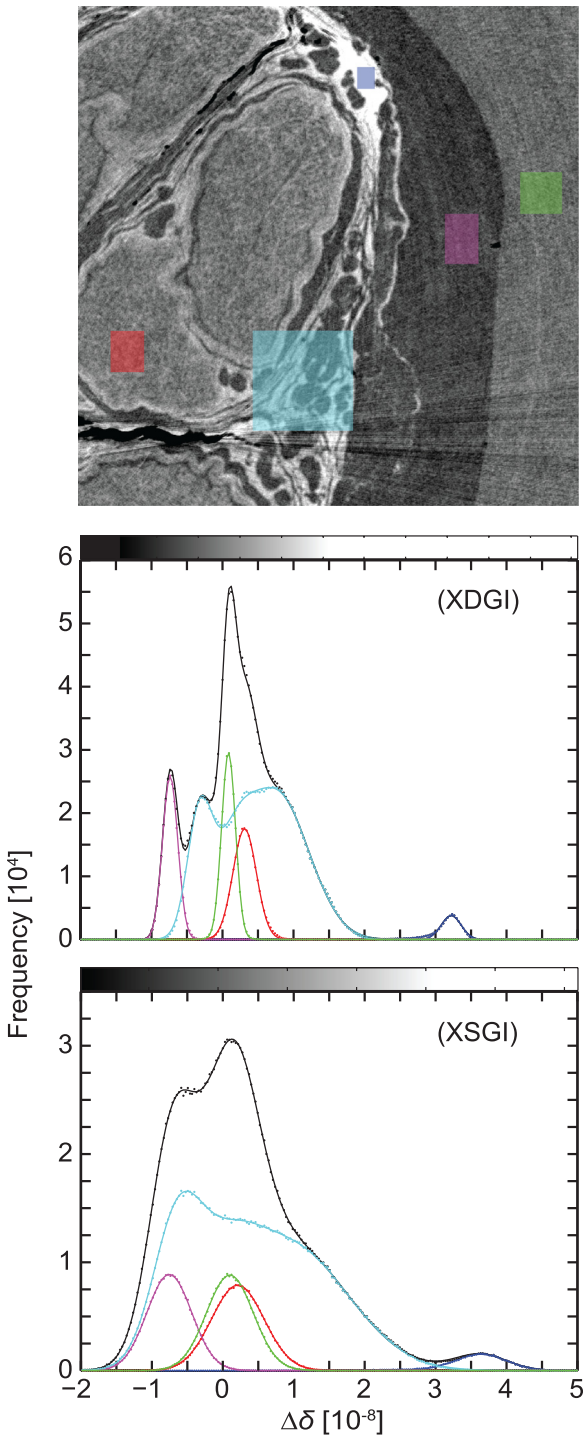

FIG. 2. Histogram for selected ROIs (top), water (green), paraffin (magenta), nerve fascicles with increased lipid composition (red), connective tissue (cyan), and connective tissue with increased formalin perfusion/dried out paraffin (blue) for XDGI (top) and XSGI (bottom), reconstructed with a binning factor of two. The corresponding histograms were fitted with Gaussians. The fitting parameters are listed in Table I and the resulting contrast-to-noise ratios are listed in Table II. The cyan curves' histograms belong to the zoom-ins in Fig. 1.

The histograms of the selected regions of interest (ROIs) of the XDGI and XSGI are shown in Fig. 2. The related mean and standard deviation values of the Gaussian distributions for selected tissues are listed in Table I. Quantitatively, we can define the contrast-to-noise ratio (CNR) for a specific feature as $|x_0^{feature} - x_0^{paraffin}|/\sigma_{paraffin}$, where x_0 denotes the

TABLE I. List of fitting parameters derived from the Gaussian fits in Fig. 2, where x_0 denotes the expectation value and σ^2 the variance of the $\Delta\delta$ values for different tissue types.

	XDGI		XSGI	
Tissue type	$x_0/10^{-8}$	$\sigma/10^{-8}$	$x_0/10^{-8}$	$\sigma/10^{-8}$
Preparation-affected connective tissue	3.22 ± 0.01	0.14 ± 0.01	3.63 ± 0.01	0.37 ± 0.01
Nerve fascicles	0.31 ± 0.01	0.16 ± 0.01	0.22 ± 0.01	0.37 ± 0.01
Water	0.09 ± 0.01	0.10 ± 0.01	0.10 ± 0.01	0.33 ± 0.01
Paraffin	−0.74 ± 0.01	0.11 ± 0.01	−0.75 ± 0.01	0.32 ± 0.01
Connective tissue I	0.76 ± 0.03	0.46 ± 0.02	0.93 ± 0.03	0.83 ± 0.02
Connective tissue II	0.15 ± 0.02	0.26 ± 0.03	0.03 ± 0.05	0.43 ± 0.04
Connective tissue III	−0.32 ± 0.01	0.17 ± 0.01	−0.65 ± 0.02	0.34 ± 0.01

expectation value of a homogeneous region and σ the corresponding standard deviation.[24] As the mean values of the peaks for both techniques are almost identical, the difference in contrast is predominantly given by the difference in the standard deviation of the paraffin peak. The findings illustrated in Fig. 3(a) show the power law dependence of the contrast-to-noise ratio on the binning factor, in comparison to the square dependence in standard absorption contrast.[21,25] The CNR was significantly lower for the XSGI, but this observed difference decreased when binning factors were increased. The selected results of the CNR analysis are listed in Table II.

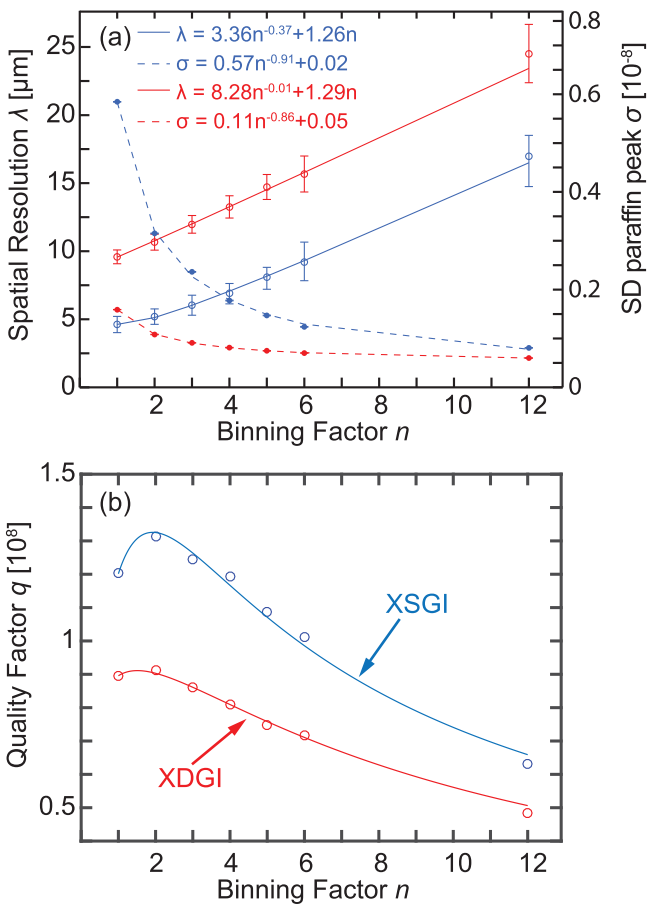

FIG. 3. (a) Spatial (dashed) and density (solid) resolution (standard deviation of the paraffin peak) versus binning factor. (b) Calculated dimensionless quality factor q versus binning factor. The fits were derived by using the fits from the upper figure. Both curves exhibit a maximum near a binning factor of two.

Spatial resolution can be defined as the intersection of the normalized modulation transfer function (MTF) with its 10 % value.[21] For the calculation, we have chosen a region at the paraffin-water interface, where the edge was almost parallel to the y-axis. In order to reduce noise effects, we applied the MTF to the median of the xz-plane over a height of around 50 μm. The results are plotted in Fig. 3(a) and confirm that XSGI provides images with higher resolution compared to ones acquired with XDGI. The spatial resolution of the XSGI was almost twice as high as that of the XDGI for the binning factors used.

Analogously to standard absorption contrast,[21] we can introduce the dimensionless quality factor $q = c \times 1/(\lambda \times \sigma^{1/3})$. For its calculation, we decided to take the paraffin width, similar to our approach to the CNR calculation, due to the homogeneity of the structure. The constant c follows directly from the proportionality of the decrement of the reflective index and the electron density, but was set to unity for the calculation of the quality factor. For both techniques, the quality factor reached its maximum for a binning factor of around two for the selected tissue (see Fig. 3(b)). From the approximate proportionality of the refractive index difference and the density difference, we received an estimation of the detection limit of the density deviation of (6.9 ± 0.7) mg/cm^3 for XDGI and (22.9 ± 0.7) mg/cm^3 for the XSGI for a binning factor of two.

In conclusion, we present in this study a quantitative comparison of the well-established XDGI and the not yet common XSGI. Despite the lower CNR of XSGI, the contrast was sufficient to identify the internal structure. Moreover, XSGI shows an improvement of the spatial resolution by a factor of about two. If the three times lower contrast in the unfiltered tomograms is sufficient for the investigation of the internal structure of the specimen, as it was in this study, XSGI is preferable to XDGI.

TABLE II. List of selected contrast-to-noise ratios calculated from the fitting parameters in Fig. 2.

	XDGI	XSGI
Water	7.55 ± 1.14	2.66 ± 0.15
Nerve fascicles	9.55 ± 1.26	3.03 ± 0.10
Affected connective tissue	36.00 ± 3.40	13.69 ± 0.43

The authors thank H. Deyhle, University of Basel, for his help with the measurements and many useful discussions, F. Beckmann, Helmholtz-Zentrum Geesthacht, for his help with the experimental set-up, as well as J. Hench and G. Schweighauser of the Neuropathology Department of the Basel University Hospital for providing the sample and helping with the special preparation required for tomography measurement.

The financial contribution of the Swiss National Science Foundation (Project Nos. 144535 and 147172) is gratefully acknowledged.

[1]I. Zanette, S. Lang, A. Rack, M. Dominietto, M. Langer, F. Pfeiffer, T. Weitkamp, and B. Müller, "Holotomography versus x-ray grating interferometry: A comparative study," Appl. Phys. Lett. **103**, 244105 (2013).
[2]S. Lang, I. Zanette, M. Dominietto, M. Langer, A. Rack, G. Schulz, G. Le Duc, C. David, J. Mohr, F. Pfeiffer, B. Müller, and T. Weitkamp, "Experimental comparison of grating- and propagation-based hard X-ray phase tomography of soft tissue," J. Appl. Phys. **116**, 154903 (2014).
[3]T. Weitkamp, A. Diaz, C. David, F. Pfeiffer, M. Stampanoni, P. Cloetens, and E. Ziegler, "X-ray phase imaging with a grating interferometer," Opt. Express **13**, 6296–6304 (2005).
[4]Y. Takeda, W. Yashiro, Y. Suzuki, S. Aoki, T. Hattori, and A. Momose, "X-ray phase imaging with single phase grating," Jpn. J. Appl. Phys. **46**, L89 (2007).
[5]M. Kagias, S. Cartier, Z. Wang, A. Bergamaschi, R. Dinapoli, A. Mozzanica, B. Schmitt, and M. Stampanoni, "Single shot x-ray phase contrast imaging using a direct conversion microstrip detector with single photon sensitivity," Appl. Phys. Lett. **108**, 234102 (2016).
[6]U. Bonse and F. Busch, "X-ray computed microtomography (μCT) using synchrotron radiation (SR)," Prog. Biophys. Mol. Biol. **65**, 133–169 (1996).
[7]A. Momose, T. Takeda, Y. Itai, and K. Hirano, "Phase-contrast X-ray computed tomography for observing biological soft tissues," Nat. Med. **2**, 473–475 (1996).
[8]G. Schulz, T. Weitkamp, I. Zanette, F. Pfeiffer, F. Beckmann, C. David, S. Rutishauser, E. Reznikova, and B. Müller, "High-resolution tomographic imaging of a human cerebellum: comparison of absorption and grating-based phase contrast," J. R. Soc., Interface. **7**, 1665–1676 (2010).
[9]S. Madduri, K. Feldman, T. Tervoort, M. Papalozos, and B. Gander, "Collagen nerve conduits releasing the neurotrophic factors gdnf and ngf," J. Controlled Release **143**, 168–174 (2010).
[10]H. Fujimaki, K. Uchida, G. Inoue, M. Miyagi, N. Nemoto, T. Saku, Y. Isobe, K. Inage, O. Matsushita, S. Yagishita, J. Sato, S. Takano, Y. Sakuma, S. Ohtori, K. Takahashi, and M. Takaso, "Oriented collagen tubes combined with basic fibroblast growth factor promote peripheral nerve regeneration in a 15 mm sciatic nerve defect rat model," J. Biomed. Mater. Res. A **105**, 8–14 (2017).
[11]B. M. Baker, A. O. Gee, R. B. Metter, A. S. Nathan, R. L. Marklein, J. A. Burdick, and R. L. Mauck, "The potential to improve cell infiltration in composite fiber-aligned electrospun scaffolds by the selective removal of sacrificial fibers," Biomaterials **29**, 2348–2358 (2008).
[12]M. Donnelley, K. S. Morgan, K. K. W. Siu, A. Fouras, N. R. Farrow, R. P. Carnibella, and D. W. Parsons, "Tracking extended mucociliary transport activity of individual deposited particles: longitudinal synchrotron X-ray imaging in live mice," J. Synchrotron Radiat. **21**, 768–773 (2014).
[13]R. P. Murrie, K. S. Morgan, A. Maksimenko, A. Fouras, D. M. Paganin, C. Hall, K. K. W. Siu, D. W. Parsons, and M. Donnelley, "Live small-animal X-ray lung velocimetry and lung micro-tomography at the australian synchrotron imaging and medical beamline," J. Synchrotron Radiat. **22**, 1049–1055 (2015).
[14]A. Hipp, F. Beckmann, P. Lytaev, I. Greving, L. Lottermoser, T. Dose, R. Kirchhof, H. Burmester, A. Schreyer, and J. Herzen, "Grating-based x-ray phase-contrast imaging at petra III," Proc. SPIE **9212**, 921206 (2014).
[15]T. Weitkamp, C. David, C. Kottler, O. Bunk, and F. Pfeiffer, "Tomography with grating interferometers at low-brilliance sources," Proc. SPIE **6318**, 63180S (2006).
[16]J. Herzen, T. Donath, F. Beckmann, M. Ogurreck, C. David, J. Mohr, F. Pfeiffer, and A. Schreyer, "X-ray grating interferometer for materials-science imaging at a low-coherent wiggler source," Rev. Sci. Instrum. **82**, 113711 (2011).
[17]M. Ruiz-Yaniz, I. Zanette, A. Sarapata, L. Birnbacher, M. Marschner, M. Chabior, M. Olbinado, F. Pfeiffer, and A. Rack, "Hard X-ray phase-contrast tomography of non-homogeneous specimens: grating interferometry *versus* propagation-based imaging," J. Synchrotron Radiat. **23**, 1202–1209 (2016).
[18]P. Modregger, B. R. Pinzer, T. Thüring, S. Rutishauser, C. David, and M. Stampanoni, "Sensitivity of X-ray grating interferometry," Opt. Express **19**, 18324–18338 (2011).
[19]A. C. Kak and M. Slaney, *Principles of Computerized Tomographic Imaging* (IEEE Press, 1988).
[20]F. Pfeiffer, O. Bunk, C. Kottler, and C. David, "Tomographic reconstruction of three-dimensional objects from hard X-ray differential phase contrast projection images," Nucl. Instrum. Methods Phys. Res., Sect. A **580**, 925–928 (2007).
[21]P. Thurner, F. Beckmann, and B. Müller, "An optimization procedure for spatial and density resolution in hard X-ray micro-computed tomography," Nucl. Instrum. Methods Phys. Res., Sect. B **225**, 599–603 (2004).
[22]See http://www.itk.org for The Insight Segmentation and Registration Toolkit (ITK), 2016.
[23]M. N. Holme, G. Schulz, H. Deyhle, T. Weitkamp, F. Beckmann, J. A. Lobrinus, F. Rikhtegar, V. Kurtcuoglu, I. Zanette, T. Saxer, and B. Müller, "Complementary x-ray tomography techniques for histology-validated 3d imaging of soft and hard tissues using plaque-containing blood vessels as examples," Nat. Protoc. **9**, 1401–1415 (2014).
[24]G. Schulz, T. Weitkamp, I. Zanette, F. Pfeiffer, M. Müller-Gerbl, C. David, and B. Müller, "Asymmetric rotational axis reconstruction of grating-based x-ray phase contrast tomography of the human cerebellum," Proc. SPIE **8506**, 850604 (2012).
[25]L. Grodzins, "Optimum energies for x-ray transmission tomography of small samples: Applications of synchrotron radiation to computerized tomography I," Nucl. Instrum. Methods Phys. Res. **206**, 541–545 (1983).